


Article

Investigation of the Stability and Hydrogen Evolution Activity of Dual-Atom Catalysts on Nitrogen-Doped Graphene

Qiansong Zhou^{1,2}, Meng Zhang³, Beien Zhu^{1,4,*} and Yi Gao^{1,4,*} 

¹ Key Laboratory of Interfacial Physics and Technology, Shanghai Institute of Applied Physics, Chinese Academy of Sciences, Shanghai 201800, China; zhouqiansong@sinap.ac.cn

² University of Chinese Academy of Sciences, Beijing 100049, China

³ Department of Physics, School of Physical Science and Technology, Ningbo University, Ningbo 315211, China; zhangmeng733@126.com

⁴ Interdisciplinary Research Center, Zhangjiang Laboratory, Shanghai Advanced Research Institute, Chinese Academy of Sciences, Shanghai 201210, China

* Correspondence: zhubeien@zjlab.org.cn (B.Z.); gaoyi@zjlab.org.cn (Y.G.)

Abstract: Single atom catalysts (SACs) have received a lot of attention in recent years for their high catalytic activity, selectivity, and atomic utilization rates. Two-dimensional N-doped graphene has been widely used to stabilize transition metal (TM) SACs in many reactions. However, the anchored SAC could lose its activity because of the too strong metal-N interaction. Alternatively, we studied the stability and activity of dual-atom catalysts (DACs) for 24 TMs on N-doped graphene, which kept the dispersion state but had different electronic structures from SACs. Our results show that seven DACs can be formed directly compared to the SACs. The others can form stably when the number of TMs is slightly larger than the number of vacancies. We further show that some of the DACs present better catalytic activities in hydrogen evolution reaction (HER) than the corresponding SACs, which can be attributed to the optimal charge transfer that is tuned by the additional atom. After the screening, the DAC of Re is identified as the most promising catalyst for HER. This study provides useful information for designing atomically-dispersed catalysts on N-doped graphene beyond SACs.

Keywords: graphene; transition metal atoms; hydrogen evolution reaction; DFT



Citation: Zhou, Q.; Zhang, M.; Zhu, B.; Gao, Y. Investigation of the Stability and Hydrogen Evolution Activity of Dual-Atom Catalysts on Nitrogen-Doped Graphene. *Nanomaterials* **2022**, *12*, 2557. <https://doi.org/10.3390/nano12152557>

Academic Editor: Lyubov G. Bulusheva

Received: 6 July 2022

Accepted: 22 July 2022

Published: 25 July 2022

Publisher's Note: MDPI stays neutral with regard to jurisdictional claims in published maps and institutional affiliations.



Copyright: © 2022 by the authors. Licensee MDPI, Basel, Switzerland. This article is an open access article distributed under the terms and conditions of the Creative Commons Attribution (CC BY) license (<https://creativecommons.org/licenses/by/4.0/>).

1. Introduction

Single atom catalysts (SACs) exhibit the maximum atomic efficiency, high selectivity, and high activity towards a variety of chemical reactions, which opens up a new frontier in the field of catalysis [1–4]. However, the practical chemical processes require a huge number of SACs, which make them easy to aggregate and form clusters owing to their high surface energies [5]. It is well known that the rational design of catalysts is a key step in catalysis research [6]. As a result, some substrates are introduced to attach single metal atoms and prevent the formation of metal clusters [7], such as Pt₁/FeO_x [8], Fe₁/SiO₂ [9], and Pt₁/C, [10]. Among them, two-dimensional defected graphene is used as the effective template to stabilize the SACs by taking advantage of a large surface area, good conductivity, good stability, and strong dispersibility [11–14]. Recently, a synergy strategy of co-doping graphene with transition-metal (TM) and nitrogen (N) atoms has been proposed to enhance the surface stability and catalytic activity simultaneously. For example, Wang et al. reported Fe SACs with triple nitrogen coordination (Fe–N₃) on graphene has excellent nitrogen reduction reaction activity [15]. Sa et al. synthesized single atom Ni anchored in N-doped graphene, which gave high performance for the carbon dioxide reduction reaction due to the dispersed highly catalytically active sites [16]. Zhong et al. studied the oxygen reduction reaction mechanism of TMs (Cr, Mn, Fe, and Co) with quadruple-coordinated nitrogen (TM–N₄) on graphene using density functional theory (DFT) calculations and

discovered that Fe/N/C had the best ORR activity [17]. Cheng et al. discovered that the single platinum atom catalysts exhibit significantly enhanced catalytic activity of the hydrogen evolution reaction, and Fang et al. uncovered that the near-free single-atom Pt possesses the favorable bonding energies with the reactants that are responsible for the superior hydrogen evolution reaction (HER) activity [18,19]. Hossain et al. and Jung et al. confirmed the excellent HER activity of single-atom Co on nitrogen-doped graphene from the perspectives of theoretical design and experimental verification [20,21]. Zang et al. demonstrated that atomically-dispersed Ni with triple nitrogen coordination (Ni–N₃) can achieve efficient hydrogen evolution reaction (HER) performance in alkaline media, which was attributed to the lower coordination number than Ni–N₄ to facilitate water dissociation and hydrogen adsorption [22].

Despite the significant progress in theory and experiments, the stability of anchored SACs possibly comes with the sacrifice of activity because of the too strong metal-support interaction. Compared with SACs, dual-atom catalysts (DACs) have emerged as a novel frontier because the synergistic effect between adjacent metal atoms can promote their catalytic activity [23]. DACs on the N-doped graphene can also be highly dispersed but have different electronic structures from SACs [24]. As the single atoms in SACs always have a stronger adsorption capacity than any other sites of support, the secondary atom is thermodynamically more likely to be captured to form DACs [25]. Therefore, DACs could form simultaneously with SACs if the practical loading of metal atoms on the surface is larger than the number of vacancies (overloading). Several studies have confirmed that using nitrogen-doped graphene as a substrate, DACs can serve as good electrocatalysts in HER [26–28]. However, there are limited studies of DACs on the N-doped graphene in the literature with respect to the studies of SACs.

In this work, we performed DFT calculations to study the stability of the TM atoms on the two-dimensional 3N-doped single-vacancy graphene (SVGN₃). A total of 24 TM elements were systematically investigated, including the third period (Ti, V, Cr, Mn, Fe, Co, Ni, and Cu), fourth period (Zr, Nb, Mo, Tc, Ru, Rh, Pd, and Ag), and fifth period (Hf, Ta, W, Re, Os, Ir, Pt, and Au). Among the 24 TM elements, 17 of them generally prefer to form the anchored SACs (TM₁–SVGN₃), while the rest of them are prone to forming DACs (TM₂–SVGN₃) instead of SACs. When the TM atoms are overloaded, all TM₂–SVGN₃ become stable. Then, the catalytic activities of SACs/DACs in the HER were predicted based on the Gibbs free energy of H adsorption [29,30]. We found 13 DACs showed higher HER activity than SACs, in which Re₂–SVGN₃ show the superior activity.

2. Materials

The spin-polarized Density Functional Theory (DFT) calculations were carried out using the exchange-correlation potential that was prescribed by Perdew–Burke–Ernzerhof (PBE) [31] and projector augmented wave (PAW) [32] methods within the Vienna ab initio simulation package (VASP) [33]. We also tested RPBE and PBE+D3 functionals with 3d elements and found that these functionals gave similar results (details in Supplementary Materials Table S1 and Figure S1). The plane-wave basis set was given a kinetic energy cutoff of 600 eV. The total energies were converged to 10^{−6} eV, and forces criteria was 0.02 eV/Å. The geometric optimization was performed using a Monkhorst–Pack grid of 3 × 3 × 1 k-points [34]. The Climbing image Nudged Elastic Band (CI–NEB) method was used to study the minimum energy path for dual-atom migration [35]. The calculated lattice parameter of graphene is 2.47 Å, which agreed with the reported theoretical and experimental results [36,37]. The optimized bulk graphene C–C bonds are 1.43 Å and the graphene supercell is then constructed based on the calculated lattice constant. In the xy plane, a 6 × 6 supercell (72 atoms) was used to eliminate the effects from the periodic structure. The distance between the graphene monolayer and its mirror copies was adjusted at 15Å in the z-axis, which was enough to preclude interactions between the two monolayers. In this work, we focus on SVGN₃ as the substrate because of its applications in experiments and the lower formation energy of single-vacancy than that of

the double-vacancy, which indicates the possibility of a single-vacancy site is high while synthesizing defect-containing graphene substrates (details in Supplementary Materials Table S2) [22,38].

The binding energy (E_b^n or E_b^G) of the TM_n on $SVGN_3$ substrate or pure graphene (G) substrate are calculated as below:

$$E_b^n = E_{TM_n-SVGN_3} - E_{SVGN_3} - nE_{TM_1} \quad (n = 1 \text{ or } 2) \quad (1)$$

$$E_b^G = E_{TM_1-G} - E_G - E_{TM_1} \quad (2)$$

where $E_{TM_n-SVGN_3}$ and E_{TM_1-G} are the total energies of TM_n-SVGN_3 and TM_1-G slab, respectively. E_{SVGN_3} is the energy of $SVGN_3$, E_G is the energy of G, E_{TM_1} is the energy of an isolated transition metal atom in the vacuum, and TM_1 and TM_2 stand for single-atom and dual-atom, respectively.

The adsorption energy ΔE_{H^*} of H atom was calculated by:

$$\Delta E_{H^*} = E_{(TM_n-SVGN_3+H)} - E_{TM_n-SVGN_3} - 1/2E_{H_2} \quad (n = 1 \text{ or } 2) \quad (3)$$

where $E_{(TM_n-SVGN_3+H)}$ represents the total energy of the TM_n-SVGN_3 systems with one adsorbed H atom, and E_{H_2} represents the energy of a gas phase H_2 molecule.

Under standard conditions, the Gibbs free energy of H adsorption, ΔG_{H^*} was obtained by the equation:

$$\Delta G_{H^*} = \Delta E_{H^*} + \Delta E_{ZPE} - T\Delta S_{H^*} \quad (4)$$

where ΔE_{ZPE} corresponds to the zero-point energy of adsorbed hydrogen and hydrogen in the gas phase H_2 molecule, and ΔS_{H^*} is the entropy difference between the adsorbed state and gas phase. The temperature (T) is 298.15 K. In this work, the E_{ZPE} and S_{H^*} values were calculated based on the vibrational frequencies through the VASPKIT [39].

3. Results and Discussion

3.1. Geometric Structures

3.1.1. Single-Atom

In Figure 1, considering the symmetry of the structure, we marked the possible adsorption sites on G and $SVGN_3$, respectively. As consistent with previous reports, the calculated C-C bond length on the optimized G is 1.42 Å, while the calculated bond lengths of C-C and C-N in the pore on the optimized $SVGN_3$ are 1.34 Å and 1.45 Å, respectively [40,41]. There are three adsorption sites on G: hollow (H), bridge (B), and top (T), and five adsorption sites on $SVGN_3$: single vacancy (S), top position of nitrogen (a), bridge position between nitrogen and nitrogen, (B') and different top positions of carbon (b or c) on the substrate.

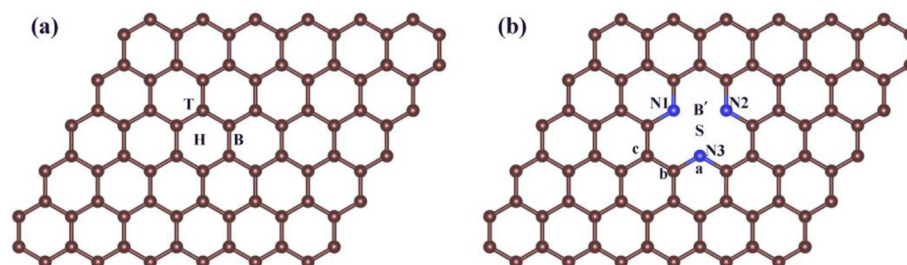


Figure 1. Color code: C, black; N, blue. (a) the three different adsorption sites (H (hollow), B (bridge), T (top)) in pure graphene; (b) in the $SVGN_3$: a stands for the top position of nitrogen, b and c stand for the top positions of carbon at different positions; B' stands for the bridge position between two nitrogen atoms; The symbol S represents the single vacancy in the substrate. The three nitrogen atoms are labeled as N1, N2, and N3, respectively.

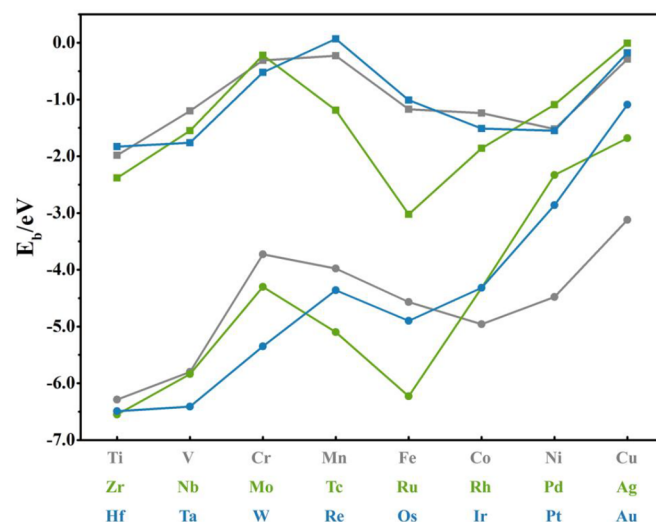
Tables 1 and 2 give the geometric parameters and binding energies of the most stable adsorption site for TM_1-G and TM_1-SVGN_3 , respectively, where M1 is a TM atom in these systems. When the M1 is adsorbed on G, the H site is the most stable adsorption site for 13 elements (Ti, V, Fe, Co, Ni, Zr, Nb, Tc, Ru, Rh, Hf, Ta, and Os); B site is the most stable adsorption site for 7 elements (Cr, Mo, Pd, Ag, W, Ir, and Pt); and the remaining elements (Mn, Cu, Re, and Au) sit on T site. Generally speaking, when the M1 is chemically adsorbed, it tends to be adsorbed at the H site, while in the case of physical adsorption, the coordination number of the M1 atom with C atoms on the surface of pure graphene decreases ($H \rightarrow B \rightarrow T$). For TM_1-SVGN_3 , the M1 is embedded in the position of the S point for all the elements. Comparing Tables 1 and 2, for elements (Cr, Mo, Pd, Ag, W, Ir, and Pt) whose B site is the best adsorption site on pure graphene, the value difference between E_b^1 and E_b^G of Pd(Pt) is relatively small, making the C-C bonds (B site) and the single-defect vacancy (S site) to single atom in Pd-SVGN₃(Pt-SVGN₃) competitive for the adsorption of a single atom, eventually resulting in one d_{M1-Nx} that is much larger than the other two. All the results are consistent with previous works [40,42–44]. As shown in Figure 2, we found much stronger E_b^1 than E_b^G , which is in line with the expectation. In addition, the binding energy of the single atom on the SVGN₃ substrate is smaller than that on the single-vacancy substrate without an N atom [14]. The binding energy is roughly positively associated with the height (h) from the M1 to the pure graphene in the TM_1-G and with the average distance (d_{M1-Nx}) from the anchored M1 to the N atom in the TM_1-SVGN_3 (details in Supplementary Materials Figures S2 and S3).

Table 1. The most stable adsorption site, binding energy (E_b^G), and M1 height from graphene (h) of TM_1-G .

	Site	E_b^G/eV	h/Å
Ti	H	−1.98	1.85
V	H	−1.20	1.85
Cr	B	−0.31	2.23
Mn	T	−0.23	2.24
Fe	H	−1.17	1.55
Co	H	−1.24	1.54
Ni	H	−1.52	1.56
Cu	T	−0.29	2.08
Zr	H	−2.38	1.98
Nb	H	−1.55	1.71
Mo	B	−0.22	2.32
Tc	H	−1.19	1.66
Ru	H	−3.02	1.73
Rh	H	−1.86	1.78
Pd	B	−1.09	2.06
Ag	B	−0.01	3.47
Hf	H	−1.83	1.93
Ta	H	−1.76	1.85
W	B	−0.52	2.22
Re	T	0.07	2.20
Os	H	−1.01	1.71
Ir	B	−1.51	1.94
Pt	B	−1.55	1.97
Au	T	−0.18	3.46

Table 2. The most stable adsorption site, binding energy (E_b^1), the distance between the anchored metal atoms (M1) and N atom (d_{M1-Nx}), and the M1 height from graphene (h) of TM_1-SVGN_3 .

	Site	E_b^1/eV	$d_{M1-N1}/\text{\AA}$	$d_{M1-N2}/\text{\AA}$	$d_{M1-N3}/\text{\AA}$	$h/\text{\AA}$
Ti	S	-6.29	1.91	1.91	1.91	1.58
V	S	-5.80	1.90	1.90	1.90	1.52
Cr	S	-3.73	1.96	1.96	1.96	1.51
Mn	S	-3.98	2.00	2.00	2.00	1.65
Fe	S	-4.57	1.78	1.78	1.78	1.23
Co	S	-4.96	1.83	1.83	1.83	1.39
Ni	S	-4.48	1.84	1.85	1.85	1.37
Cu	S	-3.12	1.89	1.89	1.89	1.51
Zr	S	-6.55	2.07	2.06	2.06	1.84
Nb	S	-5.84	1.99	1.99	1.99	1.76
Mo	S	-4.30	1.94	1.94	1.94	1.68
Tc	S	-5.10	1.91	1.91	1.91	1.59
Ru	S	-6.23	1.93	1.93	1.93	1.55
Rh	S	-4.32	2.04	2.04	2.05	1.66
Pd	S	-2.33	2.27	2.11	2.11	1.78
Ag	S	-1.68	2.31	2.31	2.31	2.05
Hf	S	-6.49	2.00	2.00	1.99	1.75
Ta	S	-6.41	1.96	1.95	1.95	1.70
W	S	-5.35	1.91	1.91	1.91	1.65
Re	S	-4.36	1.91	1.91	1.91	1.60
Os	S	-4.90	1.91	1.91	1.91	1.55
Ir	S	-4.32	2.01	2.01	2.01	1.63
Pt	S	-2.86	2.09	2.24	2.09	1.73
Au	S	-1.09	2.34	2.34	2.35	2.03

**Figure 2.** The binding energies of the TM_1-G and TM_1-SVGN_3 are shown in square and circle, respectively.

3.1.2. Dual-Atom

For dual-atoms, we defined M1 as the TM anchored at the vacancy and M2 as the additionally attached one and six initial configurations that were sampled: (Figure 3I) M2 is also at the vacancy site but on the different side of the graphene sheet; (Figure 3II) M2 is at position a, (Figure 3III) M2 is at the position b, (Figure 3IV) M2 is at the position c, (Figure 3V) M1 is at B', while M2 is at a (Figure 3VI), both atoms stay on the same side of the graphene sheet and perpendicular to the graphene sheet.

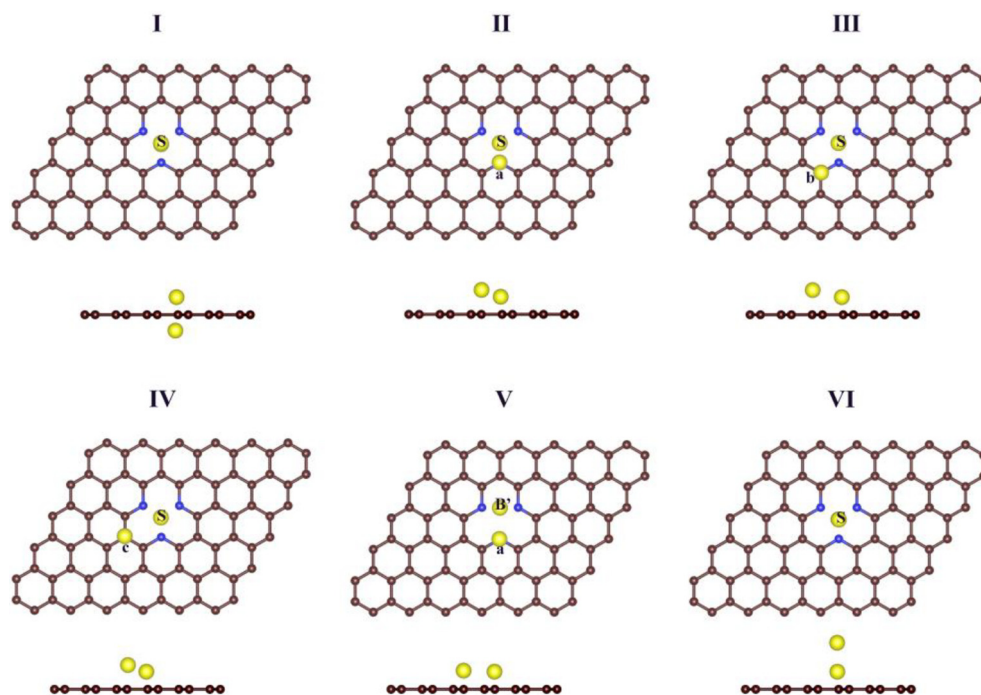


Figure 3. Color code: C, black; N, blue; TM, yellow. The six initial configurations are marked as (I–VI).

The structural and energetic parameters of DACs are summarized in Table 3. We found that there is no optimum configuration matching to Figure 3III for all the DACs. First, according to Figure 2, in the same period, the E_b^1 value of the IVB elements is the largest, so that the overloaded metal atom may also tend to bond with the single-defect vacancy, and finally the TM_2 of the group IVB elements (Ti, Zr, and Hf) takes the stable configuration as I. Second, the V_2 , Nb_2 , Rh_2 , Pd_2 , Ta_2 , and W_2 are all on the same side of the $SVGN_3$. Among them, V_2-SVGN_3 , Nb_2-SVGN_3 , and Ta_2-SVGN_3 prefer to adopt the II configuration, whereas the configurations of Rh_2-SVGN_3 and Pd_2-SVGN_3 are IV, and W_2-SVGN_3 forms a stable structure as V. Finally, the TM_2 of remaining 15 elements (Cr, Mn, Fe, Co, Ni, Cu, Mo, Tc, Ru, Ag, Re, Os, Ir, Pt, and Au) are perpendicularly adsorbed on $SVGN_3$ (configuration VI). Additionally, in the TM_2-SVGN_3 system (details in Supplementary Materials Figure S4), the average distance (d_{M1-Nx} and d_{M2-Nx}) between the dual-atoms (M1 and M2) and the N atom is related positively to the binding energy. We also tested other possible configurations and discovered that they are all unstable.

Table 3. The most stable configuration, binding energy (E_b^2), the distance between the anchored metal atoms (Mx) and N atom (d_{Mx-Nx}) (M1 denotes the first metal atom, whereas M2 denotes a second attached atom), and the metal–metal distance of M1–M2 (d_{M1-M2}).

	Configuration	E_b^2/eV	$d_{M1-N1}/\text{Å}$	$d_{M1-N2}/\text{Å}$	$d_{M1-N3}/\text{Å}$	$d_{M2-N1}/\text{Å}$	$d_{M2-N2}/\text{Å}$	$d_{M2-N3}/\text{Å}$	$d_{M1-M2}/\text{Å}$
Ti	I	−9.92	2.08	2.10	2.10	2.15	2.06	2.06	2.82
V	II	−7.79	1.95	1.95	2.04	3.48	3.48	1.98	2.03
Cr	VI	−5.70	2.07	2.07	2.07	3.26	3.27	3.28	1.51
Mn	VI	−5.75	1.96	1.96	1.96	3.82	3.78	3.81	2.28
Fe	VI	−7.21	1.85	1.85	1.85	3.43	3.44	3.43	2.06
Co	VI	−7.07	1.94	1.95	1.95	3.80	3.59	3.43	2.11
Ni	VI	−6.58	1.93	1.93	1.92	3.65	3.65	3.64	2.16
Cu	VI	−4.54	2.02	2.02	2.02	3.88	3.89	3.87	2.25

Table 3. Cont.

Configuration		E_b^2/eV	$d_{M1-N1}/\text{\AA}$	$d_{M1-N2}/\text{\AA}$	$d_{M1-N3}/\text{\AA}$	$d_{M2-N1}/\text{\AA}$	$d_{M2-N2}/\text{\AA}$	$d_{M2-N3}/\text{\AA}$	$d_{M1-M2}/\text{\AA}$
Zr	I	-11.08	2.20	2.19	2.25	2.23	2.18	2.17	3.11
Nb	II	-9.55	2.07	2.07	2.14	3.77	3.77	2.09	2.34
Mo	VI	-9.44	2.27	2.27	2.27	3.68	3.68	3.69	1.68
Tc	VI	-12.92	2.15	2.15	2.15	3.17	3.16	3.17	1.28
Ru	VI	-11.00	2.01	2.01	2.01	3.69	3.71	3.68	2.10
Rh	IV	-7.71	1.97	2.04	1.97	3.20	2.86	4.50	2.51
Pd	IV	-4.04	2.20	2.12	2.13	3.39	4.62	2.96	2.64
Ag	VI	-2.77	2.39	2.39	2.40	4.72	4.74	4.73	2.63
Hf	I	-10.71	2.16	2.16	2.19	2.19	2.16	2.16	3.07
Ta	II	-10.93	2.04	2.04	2.12	3.81	3.81	2.12	2.40
W	V	-9.77	2.04	2.04	2.82	3.25	3.25	2.19	2.11
Re	VI	-9.22	2.08	2.08	2.09	3.79	3.79	3.74	2.07
Os	VI	-10.41	2.02	2.02	2.02	3.75	3.75	3.75	2.14
Ir	VI	-9.89	2.03	2.03	2.04	3.85	3.85	3.85	2.21
Pt	VI	-7.03	2.08	2.08	2.16	4.05	4.07	4.07	2.33
Au	VI	-3.52	2.38	2.23	2.52	4.52	4.60	4.60	2.52

3.2. Stability

To evaluate the relative stability between SACs and DACs, the difference of the binding energy was calculated using the following equation:

$$\Delta E_1 = E_b^2 - 2 * E_b^1 \quad (5)$$

When ΔE_1 is negative, the anchored DAC is energetically more stable than two isolated SACs that are trapped by $SVGN_3$. As shown in Figure 4a, all the isolated SACs of 3d and 4d elements are more stable except for Mo and Tc (ΔE_1 is -0.84 eV and -2.72 eV, respectively). Among the 5d elements, the late TM elements (Re, Os, Ir, Pt, and Au) tend to form DACs instead of being dispersed into SACs, with ΔE_1 of -0.50 , -0.61 , -1.25 , -1.31 , and -1.34 eV, respectively. It is interesting to notice that when the number of 5d valence electrons (from $5d^5$ to $5d^{10}$) increases, the ΔE_1 values of these elements (Re, Os, Ir, Pt, and Au) gradually become more negative, which strongly show the DACs of these elements are more prone to forming than SACs. The investigation of the catalytic properties of these DACs are necessary.

For other elements, ΔE_1 is positive, which means the isolated SACs are preferred to form on the $SVGN_3$ when there are enough vacancies. However, as we mentioned in the Introduction, the number of TM atoms could be slightly larger than the number of vacancies in practical synthesis. When the TM atoms are overloaded, we consider the extra atoms can either disperse on the graphene surface or attach to the trapped SACs to form DACs. The relative stability was evaluated as:

$$\Delta E_2 = E_b^2 - E_b^1 - E_b^G \quad (6)$$

If ΔE_2 is negative, the DACs structure is more stable. The calculated values of ΔE_2 range from -0.55 to -6.63 eV (Figure 4b), showing the relative stability of TM_2-SVGN_3 . The absolute value of ΔE_2 generally shows that it first decreases and then increases with the increase of the atomic number of TM for the 3d and 4d elements. The more negative the value of ΔE_2 , the better the stability of TM_2-SVGN_3 . As is known, the surface energy of TM atoms will first increase and then decrease as the atomic number increases [45]. The elements in the middle of the period have more positive surface energies than the early and late TM elements in the same period [46,47], meaning the metal-metal interaction is stronger, and M2 is more likely to bond with M1 to form DACs. For example, in the 5th period elements, W, Re, and Os have the larger surface energies than the other elements, while in our calculations, W_2- , Re_2- , and Os_2-SVGN_3 possess higher relative stabilities. DACs stability can also be considered in terms of TM atoms migration energy barriers,

for example (Figure 5), Re_2 migration energy barrier in $\text{Re}_2\text{-SVG}_\text{N}_3$ is 3.16 eV, further confirming the excellent stability of $\text{Re}_2\text{-SVG}_\text{N}_3$.

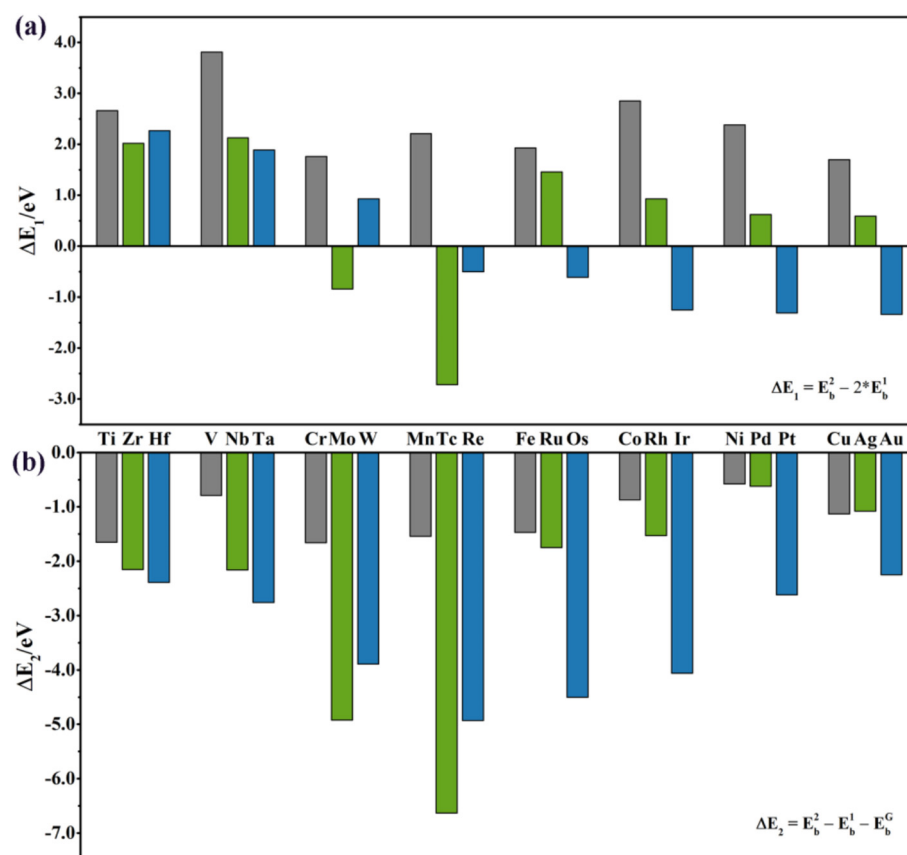


Figure 4. (a) ΔE_1 is the difference between E_b^2 and $2 * E_b^1$. (b) ΔE_2 is the difference between ΔE_2 and $(E_b^1 + E_b^G)$. (gray, green, and blue histograms represent for 3d, 4d, and 5d TM elements, respectively.)

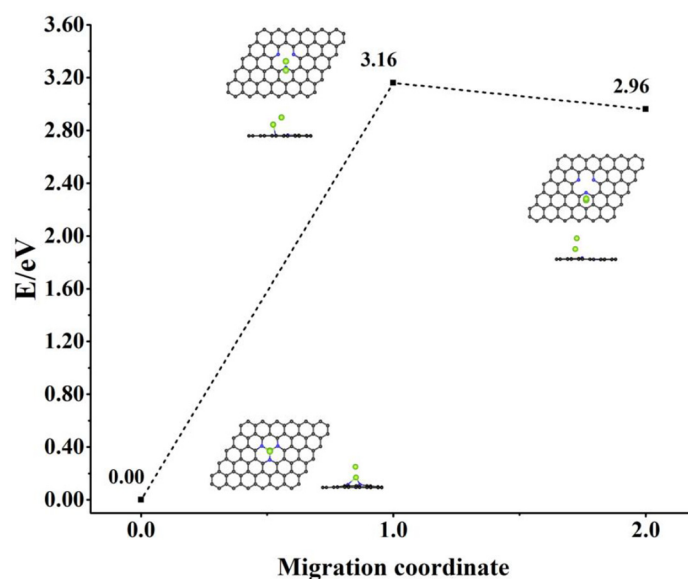


Figure 5. CI-NEB calculation for Re dual-atom migration in $\text{Re}_2\text{-SVG}_\text{N}_3$. (Color code: C, black; N, blue; Re, green).

3.3. HER Activity

With the growing worldwide energy demand and increasing environmental pressures, producing high-purity hydrogen from abundant water via an electrochemical HER

as a clean energy source is a sustainable and cost-effective option [48]. ΔG_{H^*} is well-documented as a singular activity descriptor of the HER, and there is a reported relationship between ΔG_{H^*} and HER activity in the system of graphene-supported single atom catalysts [20]. According to the Sabatier principle, the closer ΔG_{H^*} to zero ($|\Delta G_{H^*}| \leq 0.10$), the higher catalytic activity of HER [29,30,49]. If the interaction between H and the catalyst is too weak ($\Delta G_{H^*} \gg 0$), hydrogen adsorption (Volmer reaction: $H^+ + e^- + * \rightarrow H^*$, where * refers to catalysts surface) will be limited, while too strong interaction ($\Delta G_{H^*} \ll 0$) creates difficulty for the desorption step (Tafel or Heyrovsky step: $H^* + H^* \rightarrow H_2 + 2^*$ or $H^+ + H^* + e^- \rightarrow H_2 + *$) to proceed on the catalyst surface [50,51]. Based on these results, we calculated ΔG_{H^*} by considering the H adsorption on the stable SACs (TM_1-SVGN_3)/DACs (TM_2-SVGN_3) models.

The active site for HER is highly related to the adsorption site of H atom. We tested several possible configurations for the H atom adsorbed on SACs and DACs, and obtained the optimal configurations: For SACs, the most favorable adsorption sites of H is on top of the TM atoms; for DACs, the best adsorption sites of H are divided into two different situations: (1) the H bonds to the second TM atom in Ti, Cr, Zr, Mo, Tc, Ru, Os, Ir, Pt, and Hf DACs; (2) it adsorbs between the two TM atoms in V, Mn, Fe, Co, Ni, Cu, Nb, Rh, Pd, Ag, Ta, W, Re, and Au DACs. Then, ΔG_{H^*} corresponding to the most favorable adsorptions are shown in Figure 6 (details in Supplementary Materials Tables S3–S5). A total of 13 TM elements such as Ti, Mn, Fe, Mo, Rh, Ag, Hf, W, Re, Os, Ir, Pt, and Au, are predicted to have better HER activities in DACs than SACs. The results show that the DACs have better HER activities than SACs mainly in the cases where the bonding of the H atom to the TM atom is weakened in DACs. Re_2-SVGN_3 gives a ΔG_{H^*} value of -0.09 eV, which is the closest to zero among all the DACs and much closer to zero than Re_1-SVGN_3 . On the contrary, for other elements, the catalytic activity of HER will be reduced if the TM atoms form DACs. The two elements of Co and Ni exhibit excellent HER catalytic activity in the SACs, which is consistent with previous study [22,38]. In addition, we found that Pd_1-SVGN_3 can be employed as a potential element for catalyzing HER, with the ΔG_{H^*} value of -0.09 eV. These results indicate the catalytic activity of these systems can be adjusted by delicately tuning the formation of SACs or DACs.

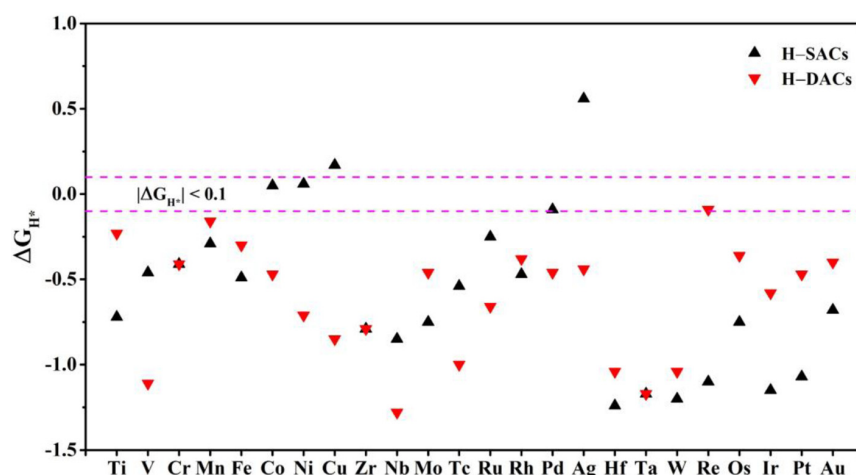


Figure 6. Gibbs free energy (ΔG_{H^*}) for HER on the SACs is represented by the black triangle, corresponding ΔG_{H^*} on the DACs is represented by the red triangle.

The intensity of H adsorption energy that is associated with charge transfer can directly affect the Gibbs free energy of H adsorption [20,52], and the Bader charge analysis can visualize charge transfer. To further investigate the HER activity of Co, Ni, Pd, and Re elements in SACs and DACs, the Bader charge analysis is performed with and without the H adsorption. As shown in Table 4, the total charge on the TMs increases upon the hydrogen adsorption. For Co, Ni, and Pd, the SACs lose fewer electrons than DACs upon H adsorption, resulting in the lower H adsorption capacities. On the contrary, the

Re SAC loses more electrons (+0.35 e) than the DAC (+0.15 e), resulting in the weaker binding strength of the H atom on Re₂. We also perform the charge density difference of Re₁-SVGN₃ and Re₂-SVGN₃ for before and after H adsorption (as presented in Figure 7), in order to further analyze the change of charge transfer during the catalytic process: (1) For Re SAC, before H adsorption, the Re single-atom is roughly positively charged due to the system's electrical neutrality, electron cloud density focusing on the N atoms in the substrate as well as the Re single-atom, and the graphene substrate being negatively charged; after H adsorption, the Re single-atom is normally negatively charged due to the system's electrical neutrality, electron cloud density focusing on the H atom and the Re single-atom, and the H atom being positively charged. (2) For Re DAC, before H adsorption, the Re dual-atom is normally negatively charged due to the system's electrical neutrality, electron cloud density focusing on the N atoms in the substrate as well as the Re dual-atom, and the graphene substrate being positively charged; after H adsorption, the Re dual-atom is still negatively charged due to the system's electrical neutrality, electron cloud density focusing on the H atom and the Re dual-atom, and the H atom being positively charged. In conclusion, we intuitively find more charge transfer for Re SAC, which is the same as our calculated results from Bader charge analysis. Thus, the smaller the electron loss upon H adsorption, the weaker the binding strength, which shifts ΔG_{H^*} towards the zero point in these cases. The different behavior of charge transfer in SACs and DACs determines the different activity.

Table 4. Bader Charges, Q(e), of the typical TMs in SACs and DACs with non-H and H adsorption. (“+” means electron loss; “-” means electron gain).

Non-H	System	Q _{M1} /e	Q _{M2} /e	Q _{M1+M2} /e	
	Co-SVGN ₃	+0.82	–	+0.82	
	Co ₂ -SVGN ₃	+0.73	–0.13	+0.60	
	Ni-SVGN ₃	+0.73	–	+0.73	
	Ni ₂ -SVGN ₃	+0.64	–0.18	+0.46	
	Pd-SVGN ₃	+0.52	–	+0.52	
	Pd ₂ -SVGN ₃	+0.47	+0.11	+0.58	
	Re-SVGN ₃	+1.00	–	+1.00	
	Re ₂ -SVGN ₃	+0.97	–0.17	+0.80	
H adsorption	System	Q _{M1} /e	Q _{M2} /e	Q _{M1+M2} /e	ΔQ /e
	Co-SVGN ₃	+0.95	–	+0.95	+0.13
	Co ₂ -SVGN ₃	+0.77	+0.08	+0.85	+0.25
	Ni-SVGN ₃	+0.74	–	+0.74	+0.01
	Ni ₂ -SVGN ₃	+0.69	+0.08	+0.77	+0.31
	Pd-SVGN ₃	+0.54	–	+0.54	+0.02
	Pd ₂ -SVGN ₃	+0.52	+0.10	+0.62	+0.04
	Re-SVGN ₃	+1.35	–	+1.35	+0.35
	Re ₂ -SVGN ₃	+1.06	–0.11	+0.95	+0.15

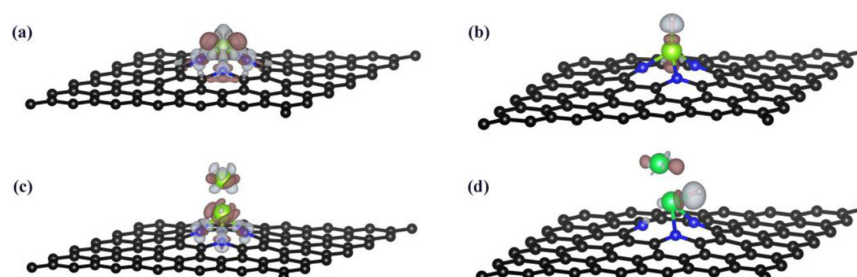


Figure 7. The charge density difference of (a,c) Re-SVGN₃, Re₂-SVGN₃ without H adsorption and (b,d) Re-SVGN₃, Re₂-SVGN₃ with H adsorption. (Color code: C, black; N, blue; Re, green; H, white; positive charge density, gray; negative charge density, dark red.).

4. Conclusions

In summary, by using DFT calculations, we systematically investigated the geometric structure, stability, and HER catalytic activity for the 3d, 4d, and 5d TM SACs and DACs on the $SVGN_3$ substrate, respectively. We conclude the DACs of Mo, Tc, Re, Os, Ir, Pt, and Au are relatively more stable than the isolated SACs. The other DACs could also form when the TM atoms are slightly overloaded on the surface. Comparing the HER reaction overpotential, 13 DACs exhibit better catalytic performance than the SACs. After screening, Re_2-SVGN_3 is predicted to be good catalysts for HER. This study shows the importance of studying DACs for atomically-dispersed catalysis. It also provides useful information to design DACs on the $SVGN_3$ surface for HER beyond SACs. Furthermore, we also found that both the electrochemical conditions and the lattice/matrix in which the metals are embedded affect the stability and HER activity of atomically-dispersed metal catalysts [51,53]. In future work, we will further consider the effect of the real environment on the stability and catalytic activity.

Supplementary Materials: The following supporting information can be downloaded at: <https://www.mdpi.com/article/10.3390/nano12152557/s1>. References [54,55] are cited in the Supplementary Materials. Table S1: Testing the binding energy (E_b) under several functional (PBE, RPBE, PBE+D3) for 3d elements; Table S2: Formation energy of $SVGN_3$ and $DVGN_4$; Table S3: zero-point energy (ZPE), and entropic correction (TS, $T = 298.15K$) of H_2 ; Table S4: The adsorption energy (ΔE_{H^+}), zero-point energy difference (ΔE_{ZPE}), and entropic correction difference ($T\Delta S_{H^+}$, $T = 298.15K$), Gibbs free energy (ΔG_{H^+}) of H–SACs at a potential $U = 0$. The ZPE and entropy of the substrate are negligible; Table S5: The adsorption energy (ΔE_{H^+}), zero-point energy difference (ΔE_{ZPE}), and entropic correction difference ($T\Delta S_{H^+}$, $T = 298.15K$), Gibbs free energy (ΔG_{H^+}) of H–DACs at a potential $U = 0$. The ZPE and entropy of the substrate are negligible; Figure S1: (a) ΔE_1 is the difference between E_b^2 and $2 * E_b^1$. (b) ΔE_2 is the difference between E_b^2 and $(E_b^1 + E_b^C)$. (Gray, green and blue histograms represent for PBE, RPBE, and PBE+D3, respectively.); Figure S2: Correlation between the height (h) from the M1 to the pure graphene and binding energy (E_b^C) in TM_1-G ; Figure S3: Correlation between the average distance (d_{M1-Nx}) from the anchored M1 to the N atom and binding energy (E_b^1) in TM_1-SVGN_3 ; Figure S4: Correlation between the average distance (d_{M1-Nx} and d_{M2-Nx}) from the dual-atoms (M1 and M2) to the N atom and binding energy (E_b^2) in TM_2-SVGN_3 .

Author Contributions: Q.Z.: Methodology, software, data curation, formal analysis, writing—original draft; M.Z.: Methodology, data curation; B.Z.: Conceptualization, validation, resources, Writing—Review & editing, supervision, project administration, funding acquisition; Y.G.: Conceptualization, writing—review & editing, supervision, project administration, funding acquisition. All authors have read and agreed to the published version of the manuscript.

Funding: The National Natural Science Foundation of China (21773287); Key Research Program of Frontier Sciences, CAS, Grant NO. ZDBS-LY-7012.

Institutional Review Board Statement: Not applicable.

Informed Consent Statement: Not applicable.

Data Availability Statement: The data presented in this study are available on request from the corresponding author.

Acknowledgments: This work was supported by the National Natural Science Foundation of China (21773287). B.Z. thanks the Youth Innovation Promotion Association, CAS and the financial support of Key Research Program of Frontier Sciences, CAS, Grant NO. ZDBS-LY-7012. All calculations were performed at National Supercomputing Center in Tianjin.

Conflicts of Interest: The authors declare that they have no known competing financial interests or personal relationships that could have appeared to influence the work reported in this paper.

References

1. Liu, L.; Corma, A. Metal Catalysts for Heterogeneous Catalysis: From Single Atoms to Nanoclusters and Nanoparticles. *Chem. Rev.* **2018**, *118*, 4981–5079. [[CrossRef](#)] [[PubMed](#)]
2. Yang, L.; Wang, X.; Wang, J.; Cui, G.; Liu, D. Graphite carbon nitride/boron-doped graphene hybrid for efficient hydrogen generation reaction. *Nanotechnology* **2018**, *29*, 345705. [[CrossRef](#)] [[PubMed](#)]
3. Jing, H.; Zhu, P.; Zheng, X.; Zhang, Z.; Wang, D.; Li, Y. Theory-oriented screening and discovery of advanced energy transformation materials in electrocatalysis. *Adv. Powder Mater.* **2021**, *1*, 100013. [[CrossRef](#)]
4. Yang, J.; Li, W.H.; Tan, S.; Xu, K.; Wang, Y.; Wang, D.; Li, Y. The Electronic Metal-Support Interaction Directing the Design of Single Atomic Site Catalysts: Achieving High Efficiency Towards Hydrogen Evolution. *Angew. Chem. Int. Ed. Engl.* **2021**, *60*, 19085–19091. [[CrossRef](#)]
5. Zhang, H.; Liu, G.; Shi, L.; Ye, J. Single-Atom Catalysts: Emerging Multifunctional Materials in Heterogeneous Catalysis. *Adv. Energy Mater.* **2018**, *8*, 1701343. [[CrossRef](#)]
6. Pan, T.; Wang, Y.; Xue, X.; Zhang, C. Rational design of allosteric switchable catalysts. *Exploration* **2022**, *2*, 20210095. [[CrossRef](#)]
7. O'Neill, B.J.; Jackson, D.H.K.; Lee, J.; Canlas, C.; Stair, P.C.; Marshall, C.L.; Elam, J.W.; Kuech, T.F.; Dumesic, J.A.; Huber, G.W. Catalyst Design with Atomic Layer Deposition. *ACS Catal.* **2015**, *5*, 1804–1825. [[CrossRef](#)]
8. Qiao, B.; Wang, A.; Yang, X.; Allard, L.F.; Jiang, Z.; Cui, Y.; Liu, J.; Li, J.; Zhang, T. Single-atom catalysis of CO oxidation using Pt1/FeOx. *Nat. Chem.* **2011**, *3*, 634–641. [[CrossRef](#)]
9. Guo, X.; Fang, G.; Li, G.; Ma, H.; Fan, H.; Yu, L.; Ma, C.; Wu, X.; Deng, D.; Wei, M.; et al. Direct, nonoxidative conversion of methane to ethylene, aromatics, and hydrogen. *Science* **2014**, *344*, 616–619. [[CrossRef](#)] [[PubMed](#)]
10. Liu, J.; Jiao, M.; Mei, B.; Tong, Y.; Li, Y.; Ruan, M.; Song, P.; Sun, G.; Jiang, L.; Wang, Y.; et al. Carbon-Supported Divacancy-Anchored Platinum Single-Atom Electrocatalysts with Superhigh Pt Utilization for the Oxygen Reduction Reaction. *Angew. Chem. Int. Ed. Engl.* **2019**, *58*, 1163–1167. [[CrossRef](#)]
11. Liu, M.; Zhang, R.; Chen, W. Graphene-supported nanoelectrocatalysts for fuel cells: Synthesis, properties, and applications. *Chem. Rev.* **2014**, *114*, 5117–5160. [[CrossRef](#)] [[PubMed](#)]
12. Guo, J.; Huo, J.; Liu, Y.; Wu, W.; Wang, Y.; Wu, M.; Liu, H.; Wang, G. Nitrogen-Doped Porous Carbon Supported Nonprecious Metal Single-Atom Electrocatalysts: From Synthesis to Application. *Small Methods* **2019**, *3*, 1900159. [[CrossRef](#)]
13. Liu, Z.; Li, S.; Yang, J.; Tan, X.; Yu, C.; Zhao, C.; Han, X.; Huang, H.; Wan, G.; Liu, Y.; et al. Ultrafast Construction of Oxygen-Containing Scaffold over Graphite for Trapping Ni²⁺ into Single Atom Catalysts. *ACS Nano* **2020**, *14*, 11662–11669. [[CrossRef](#)] [[PubMed](#)]
14. Pasti, I.A.; Jovanovic, A.; Dobrota, A.S.; Mentus, S.V.; Johansson, B.; Skorodumova, N.V. Atomic adsorption on graphene with a single vacancy: Systematic DFT study through the periodic table of elements. *Phys. Chem. Chem. Phys.* **2018**, *20*, 858–865. [[CrossRef](#)] [[PubMed](#)]
15. Wang, Y.; Cui, X.; Zhao, J.; Jia, G.; Gu, L.; Zhang, Q.; Meng, L.; Shi, Z.; Zheng, L.; Wang, C.; et al. Rational Design of Fe–N/C Hybrid for Enhanced Nitrogen Reduction Electrocatalysis under Ambient Conditions in Aqueous Solution. *ACS Catal.* **2018**, *9*, 336–344. [[CrossRef](#)]
16. Sa, Y.J.; Jung, H.; Shin, D.; Jeong, H.Y.; Ringe, S.; Kim, H.; Hwang, Y.J.; Joo, S.H. Thermal Transformation of Molecular Ni²⁺–N₄ Sites for Enhanced CO₂ Electroreduction Activity. *ACS Catalysis* **2020**, *10*, 10920–10931. [[CrossRef](#)]
17. Zhong, L.; Li, S. Unconventional Oxygen Reduction Reaction Mechanism and Scaling Relation on Single-Atom Catalysts. *ACS Catal.* **2020**, *10*, 4313–4318. [[CrossRef](#)]
18. Cheng, N.; Stambula, S.; Wang, D.; Banis, M.N.; Liu, J.; Riese, A.; Xiao, B.; Li, R.; Sham, T.K.; Liu, L.M.; et al. Platinum single-atom and cluster catalysis of the hydrogen evolution reaction. *Nat. Commun.* **2016**, *7*, 13638. [[CrossRef](#)]
19. Fang, S.; Zhu, X.; Liu, X.; Gu, J.; Liu, W.; Wang, D.; Zhang, W.; Lin, Y.; Lu, J.; Wei, S.; et al. Uncovering near-free platinum single-atom dynamics during electrochemical hydrogen evolution reaction. *Nat. Commun.* **2020**, *11*, 1029. [[CrossRef](#)] [[PubMed](#)]
20. Hossain, M.D.; Liu, Z.; Zhuang, M.; Yan, X.; Xu, G.L.; Gadre, C.A.; Tyagi, A.; Abidi, I.H.; Sun, C.J.; Wong, H.; et al. Rational Design of Graphene-Supported Single Atom Catalysts for Hydrogen Evolution Reaction. *Adv. Energy Mater.* **2019**, *9*, 1803689. [[CrossRef](#)]
21. Jung, E.; Shin, H.; Lee, B.H.; Efremov, V.; Lee, S.; Lee, H.S.; Kim, J.; Hooch Antink, W.; Park, S.; Lee, K.S.; et al. Atomic-level tuning of Co–N–C catalyst for high-performance electrochemical H₂O₂ production. *Nat. Mater.* **2020**, *19*, 436–442. [[CrossRef](#)] [[PubMed](#)]
22. Zang, W.; Sun, T.; Yang, T.; Xi, S.; Waqar, M.; Kou, Z.; Lyu, Z.; Feng, Y.P.; Wang, J.; Pennycook, S.J. Efficient Hydrogen Evolution of Oxidized Ni–N₃ Defective Sites for Alkaline Freshwater and Seawater Electrolysis. *Adv. Mater.* **2021**, *33*, e2003846. [[CrossRef](#)] [[PubMed](#)]
23. Zhang, N.; Zhang, X.; Kang, Y.; Ye, C.; Jin, R.; Yan, H.; Lin, R.; Yang, J.; Xu, Q.; Wang, Y.; et al. A Supported Pd₂ Dual-Atom Site Catalyst for Efficient Electrochemical CO₂ Reduction. *Angew. Chem. Int. Ed. Engl.* **2021**, *60*, 13388–13393. [[CrossRef](#)] [[PubMed](#)]
24. Tian, S.; Wang, B.; Gong, W.; He, Z.; Xu, Q.; Chen, W.; Zhang, Q.; Zhu, Y.; Yang, J.; Fu, Q.; et al. Dual-atom Pt heterogeneous catalyst with excellent catalytic performances for the selective hydrogenation and epoxidation. *Nat. Commun.* **2021**, *12*, 3181. [[CrossRef](#)] [[PubMed](#)]
25. Chen, Z.W.; Chen, L.X.; Yang, C.C.; Jiang, Q. Atomic (single, double, and triple atoms) catalysis: Frontiers, opportunities, and challenges. *J. Mater. Chem. A* **2019**, *7*, 3492–3515. [[CrossRef](#)]

26. Guo, X.; Gu, J.; Lin, S.; Zhang, S.; Chen, Z.; Huang, S. Tackling the Activity and Selectivity Challenges of Electrocatalysts toward the Nitrogen Reduction Reaction via Atomically Dispersed Biatom Catalysts. *J. Am. Chem. Soc.* **2020**, *142*, 5709–5721. [[CrossRef](#)]
27. Li, H.; Zhao, Z.; Cai, Q.; Yin, L.; Zhao, J. Nitrogen electroreduction performance of transition metal dimers embedded into N-doped graphene: A theoretical prediction. *J. Mater. Chem. A* **2020**, *8*, 4533–4543. [[CrossRef](#)]
28. Yang, Y.; Qian, Y.; Li, H.; Zhang, Z.; Mu, Y.; Do, D.; Zhou, B.; Dong, J.; Yan, W.; Qin, Y. O-coordinated W-Mo dual-atom catalyst for pH-universal electrocatalytic hydrogen evolution. *Sci. Adv.* **2020**, *6*, eaba6586. [[CrossRef](#)] [[PubMed](#)]
29. Nørskov, J.K.; Bligaard, T.; Logadottir, A.; Kitchin, J.R.; Chen, J.G.; Pandelov, S.; Stimming, U. Trends in the Exchange Current for Hydrogen Evolution. *J. Electrochem. Soc.* **2005**, *152*, J23. [[CrossRef](#)]
30. Greeley, J.; Jaramillo, T.F.; Bonde, J.; Chorkendorff, I.B.; Nørskov, J.K. Computational high-throughput screening of electrocatalytic materials for hydrogen evolution. *Nat. Mater.* **2006**, *5*, 909–913. [[CrossRef](#)] [[PubMed](#)]
31. Perdew, J.P.; Burke, K.; Ernzerhof, M. Generalized Gradient Approximation Made Simple. *Phys. Rev. Lett.* **1996**, *77*, 3865–3868. [[CrossRef](#)] [[PubMed](#)]
32. Kresse, G.; Joubert, D. From ultrasoft pseudopotentials to the projector augmented-wave method. *Phys. Rev. B* **1999**, *59*, 1758–1775. [[CrossRef](#)]
33. Kresse, G.; Furthmüller, J. Efficient iterative schemes for ab initio total-energy calculations using a plane-wave basis set. *Phys. Rev. B* **1996**, *54*, 11169–11186. [[CrossRef](#)]
34. Fung, V.; Hu, G.; Wu, Z.; Jiang, D.-e. Descriptors for Hydrogen Evolution on Single Atom Catalysts in Nitrogen-Doped Graphene. *J. Phys. Chem. C* **2020**, *124*, 19571–19578. [[CrossRef](#)]
35. Henkelman, G.; Uberuaga, B.P.; Jónsson, H. A climbing image nudged elastic band method for finding saddle points and minimum energy paths. *J. Chem. Phys.* **2000**, *113*, 9901–9904. [[CrossRef](#)]
36. Carlsson, J.M.; Scheffler, M. Structural, electronic, and chemical properties of nanoporous carbon. *Phys. Rev. Lett.* **2006**, *96*, 046806. [[CrossRef](#)] [[PubMed](#)]
37. Tang, Y.; Lu, Z.; Chen, W.; Li, W.; Dai, X. Geometric stability and reaction activity of Pt clusters adsorbed graphene substrates for catalytic CO oxidation. *Phys. Chem. Chem. Phys.* **2015**, *17*, 11598–11608. [[CrossRef](#)] [[PubMed](#)]
38. Zhou, Y.; Gao, G.; Li, Y.; Chu, W.; Wang, L.W. Transition-metal single atoms in nitrogen-doped graphenes as efficient active centers for water splitting: A theoretical study. *Phys. Chem. Chem. Phys.* **2019**, *21*, 3024–3032. [[CrossRef](#)] [[PubMed](#)]
39. Wang, V.; Xu, N.; Liu, J.-C.; Tang, G.; Geng, W.-T. VASPKit: A user-friendly interface facilitating high-throughput computing and analysis using VASP code. *Comput. Phys. Commun.* **2021**, *267*, 108033. [[CrossRef](#)]
40. Pašti, I.A.; Jovanović, A.; Dobrota, A.S.; Mentus, S.V.; Johansson, B.; Skorodumova, N.V. Atomic adsorption on pristine graphene along the Periodic Table of Elements—From PBE to non-local functionals. *Appl. Surf. Sci.* **2018**, *436*, 433–440. [[CrossRef](#)]
41. Zhao, C.; Wu, H. A first-principles study on the interaction of biogas with noble metal (Rh, Pt, Pd) decorated nitrogen doped graphene as a gas sensor: A DFT study. *Appl. Surf. Sci.* **2018**, *435*, 1199–1212. [[CrossRef](#)]
42. Manadé, M.; Viñes, F.; Illas, F. Transition metal adatoms on graphene: A systematic density functional study. *Carbon* **2015**, *95*, 525–534. [[CrossRef](#)]
43. Habenicht, B.F.; Teng, D.; Semidey-Flecha, L.; Sholl, D.S.; Xu, Y. Adsorption and Diffusion of 4d and 5d Transition Metal Adatoms on Graphene/Ru(0001) and the Implications for Cluster Nucleation. *Top. Catal.* **2013**, *57*, 69–79. [[CrossRef](#)]
44. Jin, C.; Cheng, L.; Feng, G.; Ye, R.; Lu, Z.H.; Zhang, R.; Yu, X. Adsorption of Transition-Metal Clusters on Graphene and N-Doped Graphene: A DFT Study. *Langmuir* **2022**, *38*, 3694–3710. [[CrossRef](#)]
45. Ruban, A.V.; Skriver, H.L.; Nørskov, J.K. Surface segregation energies in transition-metal alloys. *Phys. Rev. B* **1999**, *59*, 15990–16000. [[CrossRef](#)]
46. Vitos, L.; Ruban, A.; Skriver, H.L.; Kollár, J. The surface energy of metals. *Surf. Sci.* **1998**, *411*, 186–202. [[CrossRef](#)]
47. Lee, J.Y.; Punkkinen, M.P.J.; Schönecker, S.; Nabi, Z.; Kádas, K.; Zólyomi, V.; Koo, Y.M.; Hu, Q.M.; Ahuja, R.; Johansson, B.; et al. The surface energy and stress of metals. *Surf. Sci.* **2018**, *674*, 51–68. [[CrossRef](#)]
48. Seh, Z.W.; Kibsgaard, J.; Dickens, C.F.; Chorkendorff, I.; Nørskov, J.K.; Jaramillo, T.F. Combining theory and experiment in electrocatalysis: Insights into materials design. *Science* **2017**, *355*, eaad4998. [[CrossRef](#)] [[PubMed](#)]
49. Talib, S.H.; Lu, Z.; Yu, X.; Ahmad, K.; Bashir, B.; Yang, Z.; Li, J. Theoretical Inspection of M1/PMA Single-Atom Electrocatalyst: Ultra-High Performance for Water Splitting (HER/OER) and Oxygen Reduction Reactions (OER). *ACS Catal.* **2021**, *11*, 8929–8941. [[CrossRef](#)]
50. Santos, E.; Quaino, P.; Schmickler, W. Theory of electrocatalysis: Hydrogen evolution and more. *Phys. Chem. Chem. Phys.* **2012**, *14*, 11224–11233. [[CrossRef](#)]
51. Jovanović, A.Z.; Mentus, S.V.; Skorodumova, N.V.; Pašti, I.A. Reactivity Screening of Single Atoms on Modified Graphene Surface: From Formation and Scaling Relations to Catalytic Activity. *Adv. Mater. Interfaces* **2020**, *8*, 2001814. [[CrossRef](#)]
52. Lim, J.; Back, S.; Choi, C.; Jung, Y. Ultralow Overpotential of Hydrogen Evolution Reaction using Fe-Doped Defective Graphene: A Density Functional Study. *ChemCatChem* **2018**, *10*, 4450–4455. [[CrossRef](#)]
53. Dobrota, A.S.; Skorodumova, N.V.; Mentus, S.V.; Pašti, I.A. Surface pourbaix plots of M@N4-graphene single-atom electrocatalysts from density functional theory thermodynamic modeling. *Electrochim. Acta* **2022**, *412*, 140155. [[CrossRef](#)]

-
54. Zhang, X.; Yu, S.; Chen, H.; Zheng, W. TM atoms on B/N doped defective graphene as a catalyst for oxygen reduction reaction: A theoretical study. *RSC Adv.* **2015**, *5*, 82804–82812. [[CrossRef](#)]
 55. Liu, S.; Huang, S. Theoretical insights into the activation of O₂ by Pt single atom and Pt₄ nanocluster on functionalized graphene support: Critical role of Pt positive polarized charges. *Carbon* **2017**, *115*, 11–17. [[CrossRef](#)]